Detection of Dangerous Cornering in GNSS-Data-Driven Insurance Telematics

Johan Wahlström, Isaac Skog, *Member, IEEE*, and Peter Händel, *Senior Member, IEEE*

Abstract—We propose a framework for the detection of dangerous vehicle cornering events, based on statistics related to the no-sliding and no-rollover conditions. The input variables are estimated using an unscented Kalman filter applied to global navigation satellite system (GNSS) measurements of position, speed, and bearing. The resulting test statistic is evaluated in a field study where three smartphones are used as measurement probes. A general framework for performance evaluation and estimator calibration is presented as depending on a generic loss function. Furthermore, we introduce loss functions designed for applications aiming to either minimize the number of missed detections and false alarms, or to estimate the risk level in each cornering event. Finally, the performance characteristics of the estimator are presented as depending on the detection threshold, as well as on design parameters describing the driving behavior. Since the estimation only uses GNSS measurements, the framework is particularly well suited for smartphone-based insurance telematics applications, aiming to avoid the logistic and monetary costs associated with, e.g., on-board-diagnostics or black-box dependent solutions. The design of the estimation algorithm allows for instant feedback to be given to the driver and, hence, supports the inclusion of real-time value-added services in usage-based insurance programs.

Index Terms—UBI, insurance telematics, GNSS, vehicle lateral forces, unscented Kalman filtering.

I. INTRODUCTION

FRAMEWORKS for the detection of dangerous vehicle cornering events are foremost motivated by safety aspects. Despite efforts to stabilize rollover inclined vehicles, e.g., sport utility vehicles [1], and efforts to improve the conditions of the road surface and the quality of the tires, skidding and rollover events still play a major role in many of today's car accidents. Moreover, statistics show that even though only three percent of all vehicle crashes involve a rollover, approximately one-third of all passenger deaths are related to rollover events [2]. As of yet, no safety system exists that can completely eliminate dangers in turning events induced by excessive speeds or reckless driving. However, the industry forecasts, predicting a paradigm shift as a result of the growth of usage-based-insurance, assert that all drivers one day will be given the option to be financially compensated for safe driving.
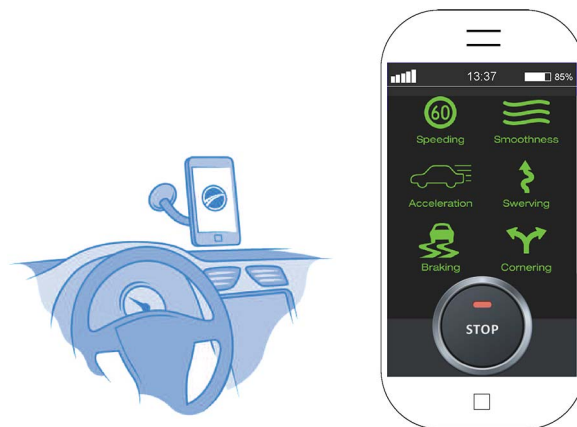
Fig. 1. Example of smartphone display used as an extension of the vehicle's dashboard. The displayed real-time feedback includes indicators of speeding, driving smoothness, acceleration, swerving, braking, and cornering.

A usage-based-insurance (UBI) is an automobile insurance where the insurer uses data on driving behavior to set the premium offered to each policyholder. The premiums are adjusted so as to reflect the individual driver risk profiles constructed by the insurer. While some commercial UBI programs are available on the market today, they are mainly based on information extracted from the cars' on-board-diagnostics (OBD) system, or from externally installed hardware components, referred to as black-boxes or aftermarket devices. The US market leader, Progressive Casualty Insurance, initialized their first UBI-program in the late 1990s, and today has approximately one and a half million policyholders signed up to their current UBI-program, Snapshot [3]. After a 30-day trial period where speed and time data are collected from the OBD system, each driver is offered to sign up for a vehicle insurance with a premium discount based on the collected data. The discount is calculated based on the total elapsed distance, how often the driver makes sudden stops, and the time of day when the data was recorded.

Currently, the commercial expansion of the UBI industry is held up by the process of acquiring data, which involves large costs related to installation, maintenance, and logistics. The use of smartphones for the collection of driving data has been identified as a promising alternative, due to the high penetration of smartphones among end-users, and the efficiency of wireless data transfer. Approximately one billion smartphones were sold in 2013, and for the first time in history the number of sold smartphones exceeded the number of sold feature phones, i.e., mobile phones only providing basic telephony. Recent estimates predict that up to 30% of all vehicles in the United States, and 60% of all vehicles in the United Kingdom, will

be insured through some type of insurance telematics (UBI by means of telecommunication) program by the year 2020 [4].

When operating as a measurement probe, the smartphone is typically mounted in the windshield (see Fig. 1), where it can provide the driver with information regarding both his driving and the surrounding traffic. (Note, however, that the smartphone of course is allowed to be picked up and moved around inside of the car.) With the use of the collected data, the insurer can individually tailor the real-time feedback given to each driver, and reward low-risk policyholders by offering them a premium discount. Commonly employed figure of merits (FoMs) in the construction of the drivers' risk profiles include measures based on speeding, driving smoothness, harsh acceleration, harsh braking, swerving, eco-driving, and harsh cornering [5].

Recent studies on smartphone-based risk assessment of driving behavior has employed GNSS sensors [6], inertial measurement units (IMUs) [7], both IMUs and GNSS sensors [8], and in addition also OBD data [9]. (For an overview of the characteristics of IMUs in smartphones, refer to [10].) The studied FoMs include speeding, cornering, harsh acceleration, and harsh braking.

The collected driving data can also be used in complementary projects with aims of societal value, such as reducing congestion and emissions [11]. Several studies has proposed the fusion of telematics data with data from vehicle detection loops (detecting vehicles passing or arriving at some fixed point) when constructing e.g., incident detectors, or estimators of expected travel times [12]–[14].

Prevailing challenges currently limiting the expansion of the insurance telematics industry include privacy considerations for end-users [15], [16], the implementation and design of attractive value added services [11], the storage of data [17], and the issue of correlating driving behavior with drivers' insurance claim history. Furthermore, the global navigation satellite system (GNSS) receivers commonly installed in smartphones are often of low quality, and the high presence of errors in the data demands a substantial use of data processing algorithms to increase the reliability of the data. Although motion sensors such as accelerometers, gyroscopes, and magnetometers, now are included in most smartphones, their potential use in telematics applications is constrained by several factors. As an example, note that high rate velocity estimates based on integration of accelerometer measurements requires an accurate estimate of the smartphone's orientation [18]. However, low-cost gyroscopes embedded in smartphones exhibit a great deal of noise, and will in a short period of time induce a noticeable drift in the estimated orientation. The estimate can be stabilized in e.g., an attitude and heading reference system (AHRS) [19], [20], which corrects the gyroscope predictions by using low-pass filtered accelerometer and magnetometer measurements to estimate the direction of the gravity vector and the magnetic north. The accuracy of the estimated orientation is degraded by, among other things, vibrations of the vehicle engine [21], accelerations of the car, and magnetic disturbances [22]. Since the AHRS updates requires measurements performed over a period long enough to eliminate the influence of most high frequency errors, but short enough to justify the assumption that the estimated quantities

are constant, performance typically drops during high dynamic movements.

Another option is to employ a GNSS-aided inertial navigation system (INS) where the errors of velocity estimates, propagated using measurements from high rate sensors, are bounded by continuous updates from GNSS measurements [20], [23]. This will generally increase the bandwidth of the estimated attitude. The estimate is however sensitive to both GNSS outages and the chosen initialization method. Typically, it is assumed that the initial state vector can be estimated during a period of zero acceleration [24], which severely limits the utility of the estimation framework in telematics applications. Since basic smartphones usually do not provide raw GNSS measurements (pseudorange, carrier-phase, or Doppler shift estimates), GNSS-aided INSs are limited to have a loosely coupled system architecture [25]. Moreover, the estimation is complicated by the fact that the smartphone is not required to be fixed inside of the car, which means that movements of the smartphone relative to the vehicle must be identified and separated from the dynamics of the vehicle itself. Due to the increased update rate and the need to estimate both sensor bias and the attitudes of the vehicle and the smartphone, the computational cost of an AHRS or a GNSS-aided INS would presumably be several orders of magnitude larger than an implementation only navigating on GNSS measurements.

The object of this paper is to present and study the accuracy of a method for the detection of dangerous vehicle cornering events, solely based on GNSS data. (Related studies utilizing measurements from e.g., IMUs or optical sensors measuring the steering angle, can be found in [26]–[28].) The paper is organized as follows: Section II derives statistics related to the no-sliding and no-rollover conditions, and use these to define a cornering event in terms of vehicle dynamics. Section III then discusses the method employed to estimate the vehicle dynamics. A framework for performance evaluation and mapping between estimated and true cornering events is provided in Section IV, and the results of the conducted field study are presented in Section V. Some final conclusions are drawn in Section VI.

II. PROBLEM FORMULATION

In this section, we will present the test statistic which is used to determine whether the driver did engage in a (dangerous) cornering event at time t_n. We begin by examining under what conditions skidding and rollover events occur. For both types of events, we will assume that the vehicle's pitch and roll angles are equal to zero, and that the driving trajectory can be locally approximated with a circle. Values of the generic variable $\mathbf{c}$ are by notation separated as measured $\tilde{\mathbf{c}}$, estimated $\hat{\mathbf{c}}$, developing in continuous time $\mathbf{c}(t)$, or developing in discrete time $\mathbf{c}_n$, where n is the index of the sampling instance t_n.

First, we derive the no-sliding condition using arguments from classical mechanics. To this end, note that the force of friction F_f exerted on the tires, is limited by the friction equation

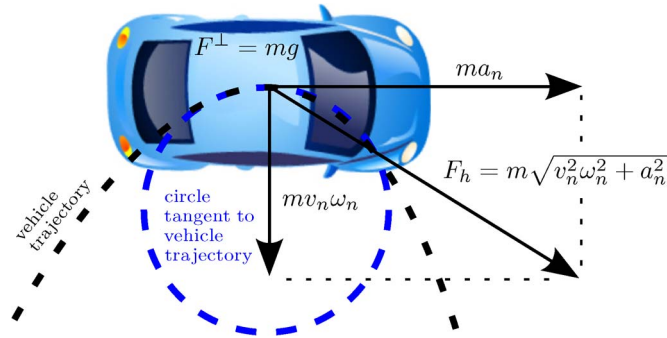$$F_f \leq F_{f,\max} \triangleq \mu F^{\perp} \qquad (1)$$

Fig. 2. To avoid a sliding event, the normal force $F^\perp$, multiplied by the coefficient of friction μ, must exceed the horizontal force F_h. This is equivalent to saying that (2) must hold at all time instants.
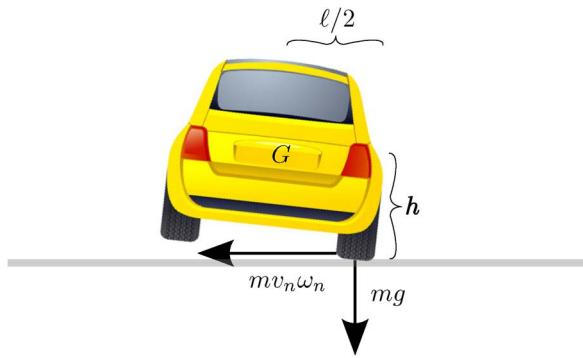

Fig. 3. To avoid a rollover event, the torque $mg\,\ell/2$ from the gravity force must exceed the torque $mv_n\omega_n h$ from the centripetal force. This is equivalent to saying that (5) must hold at all time instants.

which says that the force of friction can never exceed μ, the coefficient of friction, multiplied by the normal force $F^\perp$, exchanged between the tires and the road surface. The coefficient of friction is uniquely determined by the vehicle's speed, the properties of the tires, and the road surface. The normal force will be equal to the force of gravity on the car, i.e., $F^\perp = mg$, where m denotes the mass of the car, and g is the gravitational acceleration at the surface of the earth.

Assuming that the car at time t_n travels with speed v_n and longitudinal acceleration a_n, in a perfect circle with radius v_n/ω_n, the horizontal force F_h on the tires, can be divided into two parts (see Fig. 2). The first is the centripetal force, equal to $mv_n\omega_n$ and directed towards the center of the circle. The second is the tangential force ma_n, directed along the line tangent to the circle at the position of the vehicle at time t_n. Since these two forces are perpendicular, and since we must have $F_f = F_h$ if we are to avoid slipping, the friction equation can be rewritten as

$$T(v_n, a_n, \omega_n) \leq \mu \qquad (2)$$

where the force ratio $F_h/F^\perp$ is denoted by

$$T(v, a, \omega) \triangleq F_h/F^\perp = \frac{1}{g}\sqrt{v^2\omega^2 + a^2}. \qquad (3)$$

Correspondingly, the condition for the avoidance of a rollover can be found by studying the moment equation around G, the car's center of gravity (see Fig. 3). At the moment of a rollover,

TABLE I
TYPICAL VALUES OF THE TIRE FRICTION COEFFICIENT [35]

Speed [km/h]	Tire condition	Water depth on road surface		
		0 [mm]	1 [mm]	2 [mm]
		The coefficient of friction: μ		
50	new	0.85	0.55	0.5
50	worn†	1	0.4	0.25
90	new	0.8	0.3	0.05
90	worn†	0.95	0.1	0.05

† Tire tread depth of $1.6\,[mm]$.

the innermost wheels will have left the ground, and the normal force only operates on the outer wheels. The force has an associated lever arm of $\ell/2$ (where ℓ is the track width of the car), giving a torque of $mg\,\ell/2$. Including also the contribution from the radial force and denoting the height above ground of G by h, the total moment around G at time t_n can in equilibrium be written as

$$mg\frac{\ell}{2} - mv_n\omega_n h = 0 \qquad (4)$$

which gives us the no-rollover condition

$$T(v_n, 0, \omega_n) \leq \frac{\ell}{2h}. \qquad (5)$$

Table I shows that the kinetic tire friction coefficient is typically slightly lower than the static stability factor $\ell/2h$ (the average static stability factor among vehicle models introduced in 2003 was approximately 1.4 for passenger cars and 1.2 for SUVs [29], [30]), and hence, the no-sliding condition should be violated before the no-rollover condition. That being said, a more realistic model including e.g., normal forces or friction forces unevenly distributed among the contact points between the tires and the road surface [31], [32], nonzero pitch or roll angles [27], additional roof loads [33], or tripped rollovers [34], would complicate the analysis.

Now, we will identify cornering events by observing whether either of the statistics in (2) and (5) reach some predetermined thresholds, that is, whether the driver violates the condition

$$\mathcal{C}: \quad T(v, a, \omega) \leq \gamma_{\text{SL}} \quad \text{and} \quad T(v, 0, \omega) \leq \gamma_{\text{RO}} \qquad (6)$$

where $\gamma_{\text{SL}} = c_1 \cdot \mu$ and $\gamma_{\text{RO}} = c_2 \cdot \ell/2h$ for some constants $c_1, c_2 \in (0, \infty)$. These constants will have to be tuned to suit the needs of the particular application at hand, and to comply with the desired level of risk that should result in a cornering event. As motivated above, the study will for simplicity focus on the estimation of $T_n \triangleq T(v_n, a_n, \omega_n)$ (i.e., we will set $c_2 = \infty$). Hence, $\mathcal{C}$ is tested by first estimating the input variables as $\hat{v}_{n|n}$, $\hat{a}_{n|n}$, and $\hat{\omega}_{n|n}$, and then calculating the corresponding test statistic $\widehat{T}_n \triangleq T(\hat{v}_{n|n}, \hat{a}_{n|n}, \hat{\omega}_{n|n})$.

When there is no currently ongoing estimated cornering event for some given detection threshold γ_{SL}, the start of an event is defined to be the first time t_{n_s} for which $\widehat{T}_{n_s} > \gamma_{\text{SL}}$. Similarly, the end of an event starting at t_{n_s} is defined as the time t_{n_e}, where n_e is the largest integer such that $\widehat{T}_{n_e} > \gamma_{\text{SL}}$,

and where $\widehat{T}_n > 0.35$ for each n such that $n_s \leq n \leq n_e$. By requiring the test statistic to fall below 0.35 (which is considered to be a typical value of T while cornering in a non-aggressive manner) in between two separate detections, we are able to avoid the risk of obtaining an increasing number of detections as γ_{SL} is increased. Without this adjustment, the reference system (described in Section V-A) will often divide, what intuitively should be classified as one event, into multiple events, as the test statistic fluctuates around γ_{SL}. We will follow the convention of denoting the duration of a cornering event detected using reference data and data from a smartphone by (τ_{m_s}, τ_{m_e}) and (t_{n_s}, t_{n_e}), respectively.

Given that a cornering event has been detected, the associated estimated risk level will be defined as

$$\widehat{T}_{t_{n_s}:t_{n_e}}^{\max} \triangleq \max\{\widehat{T}_n : t_{n_s} \leq t_n \leq t_{n_e}\} \quad (7)$$

where $\{t_n\}_{n=1}^N$ are the sampling instances of the smartphone. The true risk level, denoted by $T_{\tau_{m_s}:\tau_{m_e}}^{\max}$, will be approximated by the risk level resulting from applying the analogous definition to the test statistic provided by the reference system.

III. FILTERING OF GNSS MEASUREMENTS

This section will describe the method of estimating the input variables required for the calculation of $\widehat{T}_n$. The estimation of the input variables is carried out using a Kalman filter, which renders a recursive estimation algorithm. Standard deviations are denoted by $\sigma_{(\cdot)}^2$, where the associated stochastic variable is identified by the subscript. The identity and zero matrix of size $k \times k$ are denoted by $\mathbf{I}_k$ and $\mathbf{0}_k$, respectively, while $\mathbf{0}_{k_1,k_2}$ denotes the zero matrix of size $k_1 \times k_2$.

A. State-Space Model

We begin by presenting the state-space model from which the filtering algorithm is derived. Denoting the vehicle's position and bearing by $\mathbf{p}(t) = [p^{(1)}(t) \quad p^{(2)}(t)]^{\mathsf{T}}$ and $\theta(t)$, respectively, the vehicle dynamics are modeled by

$$\dot{\mathbf{x}}_c(t) = \mathbf{f}_c\left(\mathbf{x}_c(t)\right) + \mathbf{q}(t) \quad (8)$$

where

$$\mathbf{x}_c(t) \triangleq \begin{bmatrix} p^{(1)}(t) \\ p^{(2)}(t) \\ v(t) \\ a(t) \\ \theta(t) \\ \omega(t) \end{bmatrix}, \text{ and } \mathbf{f}_c\left(\mathbf{x}_c(t)\right) \triangleq \begin{bmatrix} v(t)\cos\left(\theta(t)\right) \\ v(t)\sin\left(\theta(t)\right) \\ a(t) \\ \alpha_v a(t) \\ \omega(t) \\ \alpha_\theta \omega(t) \end{bmatrix}, \quad (9)$$

with the decay factors $\alpha_v, \alpha_\theta \in (-\infty, 0) \, [1/s]$ describing the driver characteristics. Further, $\mathbf{q}(t)$ is assumed to be Gaussian white noise, so that the covariance is $\mathrm{Cov}(\mathbf{q}(t), \mathbf{q}(\tau)) = \delta(t - \tau)\mathbf{Q}$, where

$$\mathbf{Q} \triangleq \mathrm{diag}\left(\begin{bmatrix} 0 & 0 & 0 & \sigma_{q_v}^2 & 0 & \sigma_{q_\theta}^2 \end{bmatrix}\right), \quad (10)$$

$\delta(\cdot)$ denotes the Dirac delta function, and $\mathrm{diag}(\cdot)$ denotes the matrix which has diagonal elements equal to the argument.

The GNSS position measurements $\tilde{\mathbf{p}}_n$ are typically subject to temporally correlated errors, and will be modeled by

$$\tilde{\mathbf{p}}_n = \mathbf{p}_n + \boldsymbol{\epsilon}_n + \mathbf{w}_{\mathbf{p}_n}. \quad (11)$$

The error term $\boldsymbol{\epsilon}_n$ represent a slowly varying bias, and we will use that $\boldsymbol{\epsilon}_n \approx \boldsymbol{\epsilon}_{n-1}$. The remaining error $\mathbf{w}_{\mathbf{p}_n}$ is assumed to be discrete-time zero-mean white noise with covariance $\sigma_{\mathbf{w}_p}^2 \mathbf{I}_2$. The common mode error $\boldsymbol{\epsilon}_n$ originate from atmospheric effects and clock errors, while the noncommon mode error $\mathbf{w}_{\mathbf{p}_n}$ is due to multipath propagation and receiver noise.

Since we are not interested in estimating any absolute position of the vehicle, it is convenient to work with the relative position

$$\Delta\mathbf{p}_n \triangleq \mathbf{p}_n - \mathbf{p}_{n-1}. \quad (12)$$

Note that $\widetilde{\Delta\mathbf{p}_n} \approx \Delta\mathbf{p}_n + \mathbf{w}_{\Delta\mathbf{p}_n}$ where the measurement error is $\mathbf{w}_{\Delta\mathbf{p}_n} \triangleq \mathbf{w}_{\mathbf{p}_n} - \mathbf{w}_{\mathbf{p}_{n-1}}$. Hence, by including $\Delta\mathbf{p}_n$ instead of $\mathbf{p}_n$ in the state vector, we avoid modeling $\boldsymbol{\epsilon}_n$, and will also limit the width of the temporal correlation of the measurement errors to one sample period. Using that $\mathbf{w}_{\Delta\mathbf{p}_n}$ is a moving average process of first order, we augment the state vector with the measurement errors $\mathbf{w}_{\mathbf{p}_n}$ and $\mathbf{w}_{\mathbf{p}_n-1}$, and discretize (8) as (see [36])

$$\mathbf{x}_{n+1} = \mathbf{f}(\mathbf{x}_n) + \mathbf{G}\mathbf{q}_n \quad (13)$$

where

$$\mathbf{x}_n \triangleq \begin{bmatrix} \Delta p_n^{(1)} \\ \Delta p_n^{(2)} \\ v_n \\ a_n \\ \theta_n \\ \omega_n \\ \mathbf{w}_{\mathbf{p}_n}^{(1)} \\ \mathbf{w}_{\mathbf{p}_n}^{(2)} \\ \mathbf{w}_{\mathbf{p}_{n-1}}^{(1)} \\ \mathbf{w}_{\mathbf{p}_{n-1}}^{(2)} \end{bmatrix}, \quad \mathbf{f}(\mathbf{x}_n) \triangleq \begin{bmatrix} \int_{t_n}^{t_{n+1}} v(t)\cos\left(\theta(t)\right) dt \\ \int_{t_n}^{t_{n+1}} v(t)\sin\left(\theta(t)\right) dt \\ v_n + (e^{\alpha_v \Delta t_n} - 1)/\alpha_v \, a_n \\ e^{\alpha_v \Delta t_n} a_n \\ \theta_n + (e^{\alpha_\theta \Delta t_n} - 1)/\alpha_\theta \, \omega_n \\ e^{\alpha_\theta \Delta t_n} \omega_n \\ 0 \\ 0 \\ \mathbf{w}_{\mathbf{p}_n}^{(1)} \\ \mathbf{w}_{\mathbf{p}_n}^{(2)} \end{bmatrix}, \quad (14)$$

and $\Delta t_n \triangleq t_{n+1} - t_n$. In the implementation, the integrals in the topmost rows have to be approximated in terms of $\mathbf{x}_n$, with the white process noise $\mathbf{q}_n$ adjusted accordingly. The applied procedure is presented in Appendix I together with the process noise covariance matrix $\mathbf{Q}_n \triangleq \mathrm{Cov}(\mathbf{q}_n)$ and the process noise gain matrix $\mathbf{G}$.

The measurement equation is given by

$$\tilde{\mathbf{y}}_n = \mathbf{H}\mathbf{x}_n + \mathbf{w}_n \quad (15)$$

where $\tilde{\mathbf{y}}_n \triangleq [(\widetilde{\Delta\mathbf{p}_n})^{\mathsf{T}} \quad \tilde{v}_n \quad \tilde{\theta}_n]^{\mathsf{T}}$, $\mathbf{H} \triangleq [\mathbf{H}^{(1)} \quad \mathbf{H}^{(2)}]$, $\mathbf{H}^{(1)} \triangleq \begin{bmatrix} \mathbf{I}_3 & \mathbf{0}_{3,1} & \mathbf{0}_{3,1} & \mathbf{0}_{3,1} \\ \mathbf{0}_{1,3} & 0 & 1 & 0 \end{bmatrix}$, and $\mathbf{H}^{(2)} \triangleq \begin{bmatrix} \mathbf{I}_2 & -\mathbf{I}_2 \\ \mathbf{0}_2 & \mathbf{0}_2 \end{bmatrix}$.
We will now study the measurement error covariance matrix. For ease of notation, we collect the Doppler-based measurements of speed and bearing in the vector $\widetilde{\mathbf{do}}_n \triangleq [\tilde{v}_n \quad \tilde{\theta}_n]^{\mathsf{T}}$. The exact process of calculating these measurements is typically unknown. However, given the methods presented in the literature

[37], [38], we will assume that $\widetilde{\mathbf{do}}_n$ is derived from a preceding measurement of the two-dimensional velocity $\tilde{\mathbf{v}}_n = [\tilde{v}_n^{(1)} \ \tilde{v}_n^{(2)}]$. The measurements are modeled according to $\tilde{\mathbf{v}}_n = \mathbf{v}_n + \mathbf{w}_{v_n}$, where $\mathbf{v}_n$ denotes the true velocity, and $\mathbf{w}_{v_n}$ is assumed to be white noise with covariance $\sigma_{\mathrm{w}_v}^2 \mathbf{I}_2$. Disregarding the necessary extensions of the arctan-function required to make $\theta(t)$ continuous, $\widetilde{\mathbf{do}}_n$ can be approximated by

$$\widetilde{\mathbf{do}}_n = \mathbf{f}_{\mathrm{do}}(\tilde{\mathbf{v}}_n)$$

$$\approx \mathbf{f}_{\mathrm{do}}(\mathbf{v}_n) + \frac{\partial \mathbf{f}_{\mathrm{do}}(\mathbf{v}_n)}{\partial \mathbf{v}_n}(\tilde{\mathbf{v}}_n - \mathbf{v}_n) \tag{16}$$

where $\mathbf{f}_{\mathrm{do}}(\tilde{\mathbf{v}}_n) \triangleq [\sqrt{(\tilde{v}_n^{(1)})^2 + (\tilde{v}_n^{(2)})^2} \ \ \arctan(\tilde{v}_n^{(1)}/\tilde{v}_n^{(2)})]^\mathsf{T}$ is assumed to be unbiased, and $\partial \mathbf{f}_{\mathrm{do}}(\mathbf{v}_n)/\partial \mathbf{v}_n$ denotes the Jacobian of $\mathbf{f}_{\mathrm{do}}$. We then further have

$$\mathrm{Cov}(\widetilde{\mathbf{do}}_n) \approx \sigma_{\mathrm{w}_v}^2 \frac{\partial \mathbf{f}_{\mathrm{do}}(\mathbf{v}_n)}{\partial \mathbf{v}_n} \left(\frac{\partial \mathbf{f}_{\mathrm{do}}(\mathbf{v}_n)}{\partial \mathbf{v}_n} \right)^\mathsf{T}$$

$$= \sigma_{\mathrm{w}_v}^2 \begin{bmatrix} 1 & 0 \\ 0 & 1/v_n^2 \end{bmatrix}. \tag{17}$$

As expected, the uncertainty in the measurements of bearing increases as the vehicle's speed approaches zero. Using (17), we can approximate the covariance matrix of the measurement noise by

$$\mathbf{R}_n \triangleq \mathrm{Cov}(\mathbf{w}_n) = \mathrm{diag}\left(\begin{bmatrix} 0 & 0 & \sigma_{\mathrm{w}_v}^2 & \sigma_{\mathrm{w}_v}^2/v_n^2 \end{bmatrix} \right). \tag{18}$$

Noteworthy, even though the vehicle's approximate position is needed when estimating the velocity from Doppler measurements, the resulting error dependence can be neglected since a position error of about 100 [m] only will give a velocity error in the order of 0.01 [m/s] [37].

B. Unscented Kalman Filter

The measurements are filtered using an unscented Kalman filter where the state estimates are constrained using projections [39]. As opposed to when employing an extended Kalman filter, an unscented Kalman filter allows for an implementation where constraints are applied to individual sigma points, rather than only to the navigation solution. The augmented state vector is denoted by

$$\boldsymbol{\chi}_n \triangleq \begin{bmatrix} \mathbf{x}_n \\ \mathbf{q}_n \end{bmatrix} \tag{19}$$

and the propagated sigma points are given by

$$\begin{cases} \boldsymbol{\chi}_{n|n}^{(0)} &= \hat{\boldsymbol{\chi}}_{n|n} \\ \boldsymbol{\chi}_{n|n}^{(i)} &= \hat{\boldsymbol{\chi}}_{n|n} + \eta[(\mathbf{P}_{n|n}^{(\chi)})^{1/2}]_{:,i}, \quad i \in \{1,\dots,20\} \\ \boldsymbol{\chi}_{n|n}^{(i+20)} &= \hat{\boldsymbol{\chi}}_{n|n} - \eta[(\mathbf{P}_{n|n}^{(\chi)})^{1/2}]_{:,i}, \quad i \in \{1,\dots,20\} \end{cases} \tag{20}$$

where

$$\hat{\boldsymbol{\chi}}_{n|n} \triangleq \begin{bmatrix} \hat{\mathbf{x}}_{n|n}^\mathsf{T} & \mathbf{0}_{1,10} \end{bmatrix}^\mathsf{T}, \text{ and } \mathbf{P}_{n|n}^{(\chi)} \triangleq \begin{bmatrix} \mathbf{P}_{n|n}^{(x)} & \mathbf{0}_{10} \\ \mathbf{0}_{10} & \mathbf{G}\mathbf{Q}_n\mathbf{G}^\mathsf{T} \end{bmatrix}. \tag{21}$$

Using measurements up until t_{n_2}, $\hat{\mathbf{c}}_{n_1|n_2}$ and $\mathbf{P}_{n_1|n_2}^{(c)}$ denote the estimate of $\mathbf{c}_{n_1}$ and the associated error covariance matrix, respectively. Further, $(\mathbf{M})^{1/2}$ and $[\mathbf{M}]_{:,i}$ denote the Cholesky decomposition and the i:th column of the matrix $\mathbf{M}$, respectively. The filter algorithm is presented in Algorithm 1 where the inner product is defined by

$$\langle \mathbf{c}_{n_1|n_2}, \mathbf{d}_{n_1|n_2} \rangle$$

$$\triangleq \sum_{i=0}^{40} w_i \left(\mathbf{c}_{n_1|n_2}^{(i)} - \hat{\mathbf{c}}_{n_1|n_2} \right) \left(\mathbf{d}_{n_1|n_2}^{(i)} - \hat{\mathbf{d}}_{n_1|n_2} \right)^\mathsf{T}, \tag{22}$$

and we use that $T(\mathbf{x}) \triangleq T(v, a, \omega)$ where v, a, and ω are elements in $\mathbf{x}$. The weights were set as $w_i = 1/41$ for $i \in \{1,\dots,41\}$, which further gives $\eta = \sqrt{41/2}$. Refer to [36] and [40] for details on unscented Kalman filtering.

G-forces in the vicinity of 1 g are almost exclusively attributed to sports cars with high performance tires, and most production cars never reach these levels even during aggressive cornering. (For comparison, see the skid pad numbers, i.e., the highest obtained g-forces during driving along a circle of 100 [m], collected in [41] from tests in the magazine "Car and Driver.") Therefore, all updated sigma points $\mathbf{x}_{n+1|n+1}^{(i)}$ are projected onto the space $\{\mathbf{x} : T(\mathbf{x}) \leq \mu_{\mathrm{proj}}\}$ according to

$$\mathrm{proj}\left(\mathbf{x}_{n+1|n+1}^{(i)} \right) \triangleq \underset{\mathbf{x}_{\mathrm{proj}}}{\arg\min} \left\| \mathbf{x}_{\mathrm{proj}} - \mathbf{x}_{n+1|n+1}^{(i)} \right\|_{\mathbf{P}_{n|n}^{-1}}^2$$

$$\text{s.t. } T(\mathbf{x}_{\mathrm{proj}}) \leq \mu_{\mathrm{proj}} \tag{23}$$

where $\|\mathbf{x}\|_{\mathbf{M}}^2 \triangleq \mathbf{x}^\mathsf{T}\mathbf{M}\mathbf{x}$. Note that this ensures that $T(\hat{\mathbf{x}}_{n+1|n+1}) \leq \mu_{\mathrm{proj}}$ since T is convex. The projection can be found by numerical means using gradient-based methods. The choice of only applying the constraint to *updated* sigma points has previously been motivated in [42] and references therein.

The parameter μ_{proj} describes the trade-off between, on the one hand, minimizing the risk of incorrectly altering the estimates, and on the other hand, utilizing the implicit outlier detector resulting from the use of (23). In the implementation, we used $\mu_{\mathrm{proj}} = 0.9$ which is a rather conservative choice given that the detection threshold typically will be chosen far below this value. In light of the limitations implied by Table I, a more refined implementation, applied to driving under more varied sets of circumstances than what is described in Section V, would in all probability benefit from letting μ_{proj} be dependent on the vehicle's speed or the weather.

Algorithm 1: Estimation of Vehicle Dynamics

1: Initialize $\hat{\mathbf{x}}_{1|1}$ and $\mathbf{P}_{1|1}$.

2: **for** $n = 1 : N$ **do**

3:    Generate $\{\boldsymbol{\chi}_{n|n}^{(i)}\}_{i=0}^{40}$ according to (20).

4:    $\mathbf{x}_{n+1|n}^{(i)} = \mathbf{f}(\mathbf{x}_{n|n}^{(i)}) + \mathbf{q}_{n|n}^{(i)}$

5:    $\hat{\mathbf{x}}_{n+1|n} = \sum_{i=0}^{40} w_i \mathbf{x}_{n+1|n}^{(i)}$

6:    $\mathbf{y}_{n+1|n}^{(i)} = \mathbf{H}\mathbf{x}_{n+1|n}^{(i)}$

7:    $\hat{\mathbf{y}}_{n+1|n} = \sum_{i=0}^{40} w_i \mathbf{y}_{n+1|n}^{(i)}$

8:    $\mathbf{P}_{n+1|n}^{(y)} = \langle \mathbf{y}_{n+1|n}, \mathbf{y}_{n+1|n} \rangle + \mathbf{R}_n$

9:    $\mathbf{P}_{n+1|n}^{(xy)} = \langle \mathbf{x}_{n+1|n}, \mathbf{y}_{n+1|n} \rangle$

10:   $\mathbf{K}_n = \mathbf{P}_{n+1|n}^{(xy)} (\mathbf{P}_{n+1|n}^{(y)})^{-1}$

11:   $\mathbf{x}_{n+1|n+1}^{(i)} = \mathbf{x}_{n+1|n}^{(i)} + \mathbf{K}_n(\tilde{\mathbf{y}}_{n+1} - \mathbf{y}_{n+1|n}^{(i)})$

12:   $\hat{\mathbf{x}}_{n+1|n+1} = \sum_{i=0}^{40} w_i \, \text{proj}(\mathbf{x}_{n+1|n+1}^{(i)})$

13:   $\mathbf{P}_{n+1|n+1}^{(x)} = \langle \mathbf{x}_{n+1|n+1}, \mathbf{x}_{n+1|n+1} \rangle$

14:   $\widehat{T}_{n+1} \triangleq T(\hat{\mathbf{x}}_{n+1|n+1})$

15: **end for**

All steps in Algorithm 1 referring to a sigma point i are looped over all sigma points.

C. Filter Tuning

Assuming that the accuracy of the Doppler measurements is fairly similar among different smartphone models, we will use $\sigma_{w_v}^2 = (0.2\,[\text{m/s}])^2$ [43]. Likewise, we set $\sigma_{w_p}^2 = (1.5\,[\text{m/s}])^2$. (Note that this only corresponds to the proportion of the position errors which are temporally independent.) The decay factors are typically hard to estimate from data, and will be fixed at $\alpha_v = -0.5\,[1/s]$ and $\alpha_\theta = -0.1\,[1/s]$. Since cornering events are characterized by relatively dynamic driving, this should be reflected in the model parameters. While a small value on α_v correspond to aggressive driving, α_v is limited from below by the bandwidth of the modeled car dynamics (which typically is less than 2 [Hz] [25]).

The process noise parameters σ_{q_v} and σ_{q_θ} are considered to be design parameters and their influence on the estimator is studied in the subsequent section. The appropriate value set on the parameter σ_{q_v}, describing the smoothness of the ride in terms of longitudinal acceleration, will be dependent on the driver, the intended application, etc. Similarly, σ_{q_θ} will to a large extent depend on the road type and the chosen speed. We will study values in the intervals $0 < \sigma_{q_v} \leq 0.8\,[\text{m/s}^2 \cdot \sqrt{\text{Hz}}]$ and $0 < \sigma_{q_\theta} \leq 1\,[1/\text{s} \cdot \sqrt{\text{Hz}}]$.

IV. FRAMEWORK FOR PERFORMANCE EVALUATION

We will now describe the general methodology used to evaluate the performance of the estimator $\widehat{T}_n$. This will provide a common ground for the performance evaluation in Section V, and illustrate how the study can be extended based on the intended application. The presented framework can be used to compare the performance of any given estimators of T_n, or to calibrate a parameterized estimator.
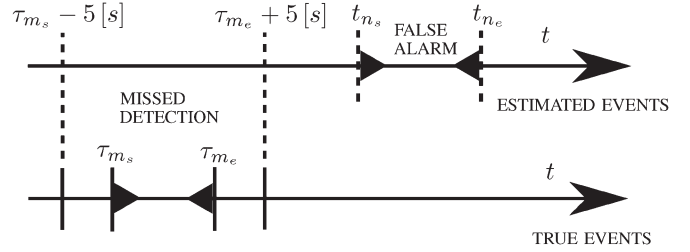

Fig. 4. An estimated event with duration (t_{n_s}, t_{n_e}) can only be mapped to a true event with duration (τ_{m_s}, τ_{m_e}) if $t_n \in (\tau_{m_s} - 5\,[\text{s}], \tau_{m_e} + 5\,[\text{s}])$ for some $t_n \in (t_{n_s}, t_{n_s})$. The mapping between estimated and true events is performed so as to bijectively map the largest possible number of events.

We first specify how to map the detections provided by a smartphone with those provided by the reference system (considered to be the true cornering events). Definitions of a missed detection and a false alarm will then follow in a straightforward manner. The objective of the mapping is to link each estimated event with the underlying physical event, if any, that has been detected. After calculating the start and end points of each cornering event, a subset of the events provided by a smartphone is bijectively mapped onto the events provided by the reference system. The mapping is constructed so as to map the largest possible subset of events, subject to the constraint that each event with duration (t_{n_s}, t_{n_e}) only can be mapped to an event with duration (τ_{m_s}, τ_{m_e}) if $t_n \in (\tau_{m_s} - 5\,[\text{s}], \tau_{m_e} + 5\,[\text{s}])$ for some $t_n \in (t_{n_s}, t_{n_e})$ (see Fig. 4). The events detected by a smartphone and the reference system which has not been mapped are considered to be false alarms and missed detections, respectively.

Now, consider a generic driving trip with data collected at the sampling instances $\{t_n\}_{n=1}^N$. The vehicle dynamics and the sensor errors (together with sampling instances) of the trip are described by the stochastic variables Λ_1 and Λ_2, respectively. Their joint probability density function (pdf) is denoted by $p_{\Lambda_1, \Lambda_2}(\lambda_1, \lambda_2)$. The Bayesian risk $\mathfrak{R}(\Theta)$ (where Θ denotes the parameter set describing the parameterization of the estimator $\widehat{T}_n$) associated with the estimator $\widehat{T}_n(\Theta; \Lambda_1; \Lambda_2)$ is now defined as

$$
\begin{aligned}
\mathfrak{R}(\Theta) &\triangleq \mathbb{E}\left[L\left(\left\{ \widehat{T}_n(\Theta; \Lambda_1; \Lambda_2) \right\}_{n=1}^N, \{T_n(\Lambda_1)\}_{n=1}^N \right) \right] \\
&= \int L\left(\{\widehat{T}_n\}_{n=1}^N, \{T_n\}_{n=1}^N \right) p_{\Lambda_1, \Lambda_2}(\lambda_1, \lambda_2) d\lambda_1 d\lambda_2
\end{aligned}
\tag{24}
$$

where L is a loss function adjusted to the insurers preferences. The pdf $p_{\Lambda_1, \Lambda_2}(\lambda_1, \lambda_2)$ will in practice have to be estimated from empirical data, and will inevitably be subject to design choices related to driving behavior, road type, the chosen smartphone, etc. Note that we have deliberately separated the parameters in Θ, describing the driving behavior, from Λ_1, to emphasize that the true vehicle dynamics are not generated from (8).

The performance evaluation in this article will be limited to studies of the estimator presented in Section III, in terms of $\mathfrak{R}(\sigma_{q_v}, \sigma_{q_\theta})$. The Bayesian risk will be estimated by

TABLE II
SUMMARY OF THE DATA USED IN THE FIELD STUDY

Elapsed time [min]	31
Elapsed distance [km]	17
Number of events with $T^{max}_{\tau_{m_s}:\tau_{m_e}} > 0.35$	40
Number of events with $T^{max}_{\tau_{m_s}:\tau_{m_e}} > 0.5$	29
Number of events with $T^{max}_{\tau_{m_s}:\tau_{m_e}} > 0.65$	21
Number of events with $T^{max}_{\tau_{m_s}:\tau_{m_e}} > 0.75$	7

considering the available reference data to be representative of $p_{\Lambda_1, \Lambda_2}(\lambda_1, \lambda_2)$, i.e., by using that $\mathfrak{R}(\Theta) \approx \bar{L}(\Theta)$, where

$$\bar{L}(\Theta) \triangleq 1/M \sum_{j=1}^{M} L\left(\left\{\widehat{T}_n\left(\Theta; \Lambda_1; \Lambda_2^{(j)}\right)\right\}_{n=1}^{N}, \{T_n(\Lambda_1^*)\}_{n=1}^{N}\right),$$
(25)

M denotes the number of smartphones, Λ_1^* represents the outcome of Λ_1 provided by the reference data, and $\Lambda_2^{(j)}$ denotes the sensor errors in the measurements from smartphone j. $T_n(\Lambda_1^*)$ will be approximated by the corresponding estimate provided by the reference system.

We will study three different loss functions, the first being defined as

$$L_{\text{MDFA}} = d \cdot MD + (1 - d) \cdot FA$$
(26)

with $d \in [0, 1]$, and where MD and FA are the number of missed detections and false alarms, respectively, divided by the total number of events. Moreover, assuming that the detected event with duration (t_{n_s}, t_{n_e}) has been mapped to the true event with duration (τ_{m_s}, τ_{m_e}), we introduce the loss functions

$$L_{\text{RMSE}} = \sqrt{\mathbb{E}\left[\left(\widehat{T}^{\max}_{t_{n_s}:t_{n_e}} - T^{\max}_{\tau_{m_s}:\tau_{m_e}}\right)^2\right]},$$
(27)

$$L_{\text{BIAS}} = \mathbb{E}\left[\widehat{T}^{\max}_{t_{n_s}:t_{n_e}} - T^{\max}_{\tau_{m_s}:\tau_{m_e}}\right],$$
(28)

where the expectation is taken over all true events detected by the reference system. If a smartphone did not detect a specific event with duration (τ_{m_s}, τ_{m_e}), $\widehat{T}^{\max}_{t_{n_s}:t_{n_e}}$ is defined as the maximum $\widehat{T}_n$ such that $t_n \in (\tau_{m_s} - 5 \text{ [s]}, \tau_{m_e} + 5 \text{ [s]})$ and where $t_n \notin (t_{n_s}, t_{n_e})$ for any detection of the smartphone with duration (t_{n_s}, t_{n_e}).

V. FIELD STUDY

A. Experimental Specification

The estimation framework presented in Section III was applied to 31 minutes of data collected during aggressive driving under normal road conditions (see Table II). Reference data was collected using a Microstrain 3DM-GX3-35, which includes an IMU and a GNSS sensor with update rates of 100 [Hz] and 4 [Hz], respectively. The IMU and GNSS data were then fused
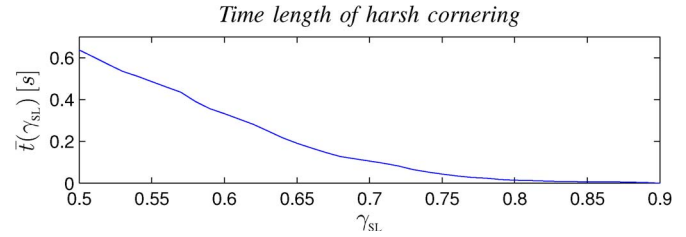

Fig. 5. The average length of time during which the test statistic exceeds γ_{SL}.

in a GNSS-aided INS, from which the force ratio $F_h/F^\perp$ was calculated (estimated from accelerometer measurements after subtraction of the gravitational acceleration and the estimated sensor bias). To minimize the influence of high frequency errors due to sensor noise, inadequate separation of the gravitational and spatial acceleration, etc., the resulting estimate of T was low-pass filtered with a cut-off frequency of 1/2 [Hz]. Data was simultaneously collected from GNSS sensors in the three Android phones Samsung Galaxy S3, Samsung Galaxy Xcover 2 (abbreviated X2), and Samsung Galaxy S4.

Fig. 5 shows the average length of time $\bar{t}(\gamma_{\text{SL}})$ during which the test statistic T_n, calculated using the reference system, stays above the detection threshold γ_{SL} after exceeding it (note that this is not the average time length of a cornering event since T_n is not required to fall below 0.35 in between two calculations of time length). It can be seen that $\bar{t}(\gamma_{\text{SL}})$ decreases in a linear fashion as $0.5 \leq \gamma_{\text{SL}} \leq 0.7$. Due to the comparatively low update rate of the smartphones (1 [Hz]), the resulting test statistic will often fail to capture short events of harsh cornering, and the risk level of detected events will tend to be underestimated. The estimated risk level can be increased by the use of a larger process noise variance, however, this is done at the expense of resistance to false alarms.

Since deliberate attempts were made to reach large g-forces, the exact average time lengths displayed in Fig. 5 should not be interpreted as typical of normal driving.

B. Performance Evaluation

Since there is no known industry standard for the detection threshold γ_{SL}, we will study thresholds in the interval $0.5 \leq \gamma_{\text{SL}} \leq 0.75$. According to the authors' experience, this corresponds to values which are typically obtained during what intuitively should be classified as aggressive driving.

An indication of the performance that can be expected is given in Table III, which shows the obtained missed detections and false alarms for different thresholds, with the design parameters fixed at $\sigma_{q_v} = 0.4$ [m/s$^2 \cdot \sqrt{\text{Hz}}$] and $\sigma_{q_\theta} = 0.4$ [1/s $\cdot \sqrt{\text{Hz}}$]. For detection thresholds in the range of $0.5 \leq \gamma_{\text{SL}} \leq 0.6$, the sum of missed detections and false alarms is around 40% of the total number of cornering events. For higher thresholds, the performance deteriorates (the large fluctuations among the different smartphones at these thresholds can be related to both the worsened performance of the detector, and the smaller number of true events). However, we expect these risk levels to be less relevant during day-to-day driving (see the discussion on the highest obtained g-forces in Section III-B).

TABLE III
MISSED DETECTIONS AND FALSE ALARMS

γ_{SL}	S3	X2	S4	Average	Number of events
	Missed detections [%] (L_{MDFA} with $d=1$)				
0.5	7	31	0	13	29
0.55	17	48	14	26	28
0.6	24	44	12	27	26
0.65	37	47	26	37	21
0.7	62	38	31	44	12
0.75	67	17	33	39	7
	False alarms [%] (L_{MDFA} with $d=0$)				
0.5	24	7	34	22	29
0.55	14	3	24	14	28
0.6	12	4	24	13	26
0.65	21	11	47	26	21
0.7	38	23	69	44	12
0.75	100	83	150	111	7
	(*Missed detections* + *False alarms*)/2 [%] (L_{MDFA} with $d=1/2$)				
0.5	16	19	17	17	29
0.55	16	26	19	20	28
0.6	18	24	18	20	26
0.65	29	29	37	32	21
0.7	50	31	50	44	12
0.75	83	50	92	75	7

Missed detections and false alarms as a percentage of the number of events, with $\sigma_{q_v} = 0.4\,[m/s^2 \cdot \sqrt{Hz}]$ and $\sigma_{q_\theta} = 0.4\,[1/s \cdot \sqrt{Hz}]$.

The performance of the estimator, as depending on the detection threshold, is further illustrated by the receiver operating characteristics (ROC) displayed in Fig. 6. The ROC with $\gamma_{\text{SL}} = 0.5$ is identical to the ROC with $\gamma_{\text{SL}} = 0.55$ (the latter threshold only results in one less true cornering event than the former). Once again, the performance is seen to be comparable for thresholds in the range of $0.5 \leq \gamma_{\text{SL}} \leq 0.6$, but then declines as the threshold is increased. Note that, as opposed to all other studies in this section which employs the same threshold for estimated and true events, each curve in Fig. 6 is obtained by fixing the threshold for the true events at γ_{SL}, while varying the threshold for the estimated events.

Now, consider Fig. 7(a), where the missed detections, averaged over the three smartphones, are displayed as a function of the threshold. It can be seen that the number of missed detections to some extent can be decreased by increasing the value of σ_{q_θ}. (The parameter σ_{q_θ} determines the well-known trade-off between dynamic response and noise resistance as-
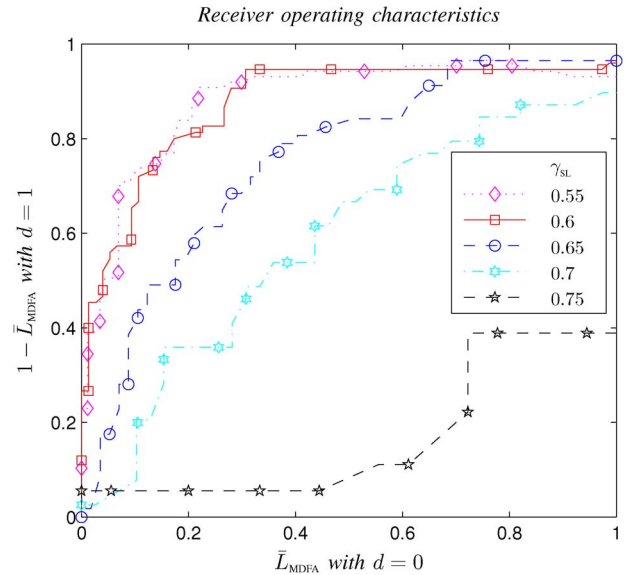

Fig. 6. Receiver operating characteristics of the detector with $\sigma_{q_v} = 0.4\,[\text{m/s}^2 \cdot \sqrt{\text{Hz}}]$ and $\sigma_{q_\theta} = 0.4\,[1/\text{s} \cdot \sqrt{\text{Hz}}]$.

sociated with the measurements of bearing, and hence, to a large extent also controls the estimated angular velocity $\hat{\omega}_{n|n}$.) However, as seen in Fig. 7(b) which shows the corresponding false alarms, this is done at the expense of a larger number of false alarms. The collected data indicate that the total sum of missed detections and false alarms stays approximately the same at smaller thresholds (see Fig. 7(c)).

In Fig. 8(a), we study the missed detections as depending on both σ_{q_v} and σ_{q_θ}, with the detection threshold fixed at 0.6. Note that the number of missed detections approaches 100% as σ_{q_θ} approaches 0, that is, when the filter has a large resistance to sudden steering maneuvers. Similarly, Fig. 8(b) shows that the number of false alarms decreases to zero as σ_{q_θ} approaches 0. Disregarding the above mentioned examples, the performance is robust with respect to the design parameters, and the two plots for which $\sigma_{q_v} = 0.4\,[\text{m/s}^2 \cdot \sqrt{\text{Hz}}]$ and $\sigma_{q_v} = 0.8\,[\text{m/s}^2 \cdot \sqrt{\text{Hz}}]$ display no strong dependence on neither of the parameters (see also the sum of missed detections and false alarms in Fig. 8(c)). Since there is a large range of values of σ_{q_v} and σ_{q_θ} with comparable performance, parameter calibration is expected to be straightforward in practical implementations.

Fig. 9(a) shows that the root mean square error of the estimated risk level is around 0.12, and hence, the normalized root mean square error is slightly above 10%. Moreover, the bias of the estimated risk level is essentially zero (see Fig. 9(b)), disregarding the previously mentioned case when σ_{q_θ} approaches zero.

VI. CONCLUDING REMARKS

This paper has presented a framework for the detection of dangerous vehicle cornering events, well-suited for smartphone-based insurance telematics applications. The ability to detect cornering events exceeds the capacity of current telematics solutions based on on-board-diagnostics, and enables both new ways to differentiate among drivers and new
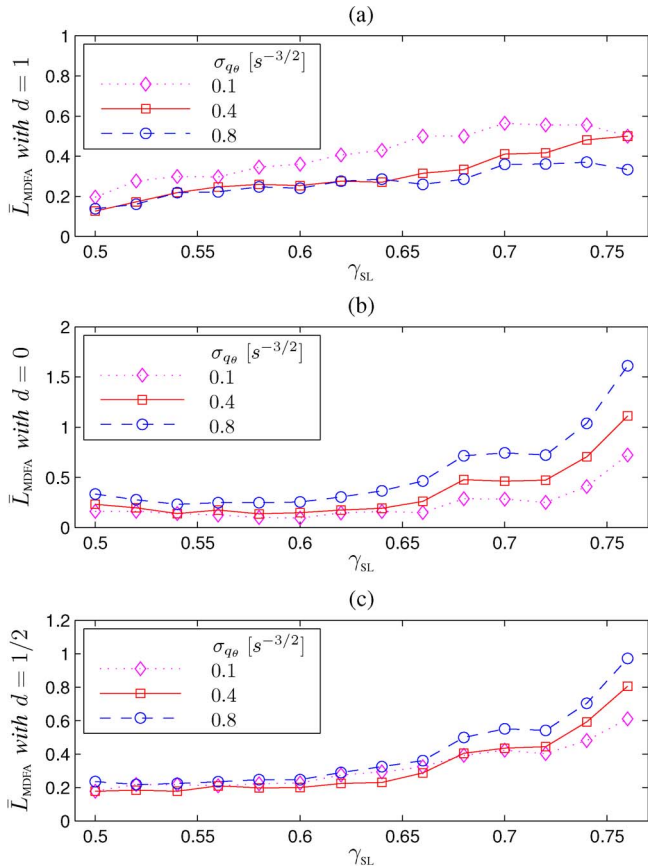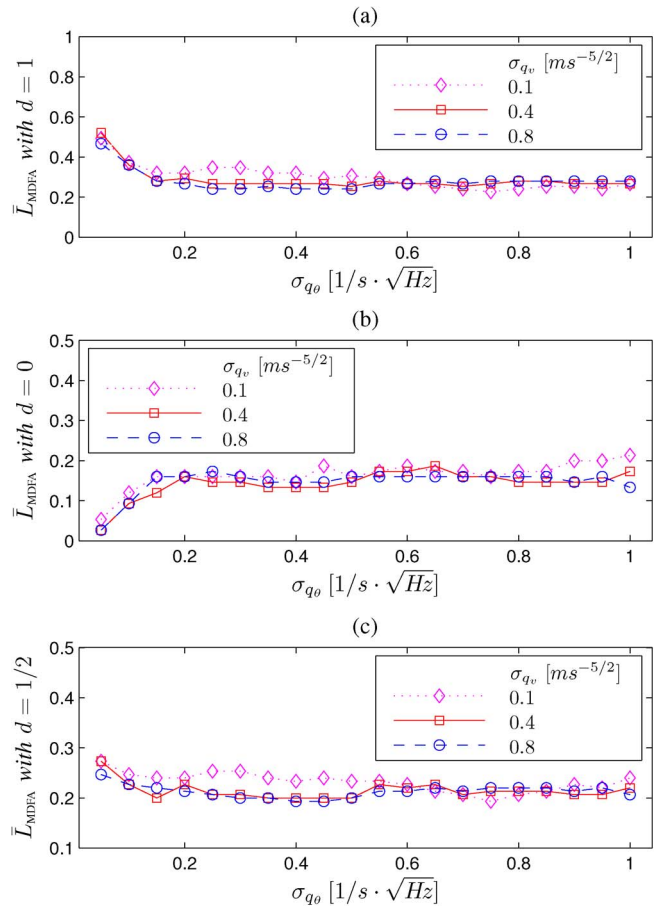
Fig. 7. Missed detections (a), false alarms (b), and the sum of missed detections and false alarms (c), divided by the total number of true cornering events. The process noise variance of the vehicle speed was set to $\sigma_{q_v} = 0.4\,[\text{m/s}^2 \cdot \sqrt{\text{Hz}}]$.

Fig. 8. Missed detections (a), false alarms (b), and the sum of missed detections and false alarms (c), divided by the total number of true cornering events. The detection threshold was set to $\gamma_{\text{SL}} = 0.6$.

Fig. 9. Average root mean square error (a) and average bias (b) of the estimated risk level. The detection threshold was set to $\gamma_{\text{SL}} = 0.6$.

value added services. The detection is based on a continuously updated test statistic estimated using an unscented Kalman filter applied to GNSS measurements of position, speed, and bearing.

A general framework for performance evaluation and estimator calibration was presented as depending on a generic loss function. Three loss functions were introduced: the first designed for an application aiming to minimize the number of missed detection and false alarms of cornering events; and the other two designed for the estimation of the risk level of a cornering event.

The performance of the estimator was evaluated in a field study where data was collected from three smartphones and a reference system utilizing high rate sensors. It was shown that the expected number of missed detections and false alarms sum up to around 40% of the total number of cornering events, while the estimated risk level has a normalized root mean square error of approximately 10%. However, the performance deteriorates as the estimator is applied to the cornering events with the largest g-forces. This can be related to the short length of time (as compared to the update rate of smartphones) during which forces in this range typically are exerted.

The performance of the estimator was shown to be robust with respect to the design parameters, and hence, parameter calibration is expected to be straightforward in practical implementations.
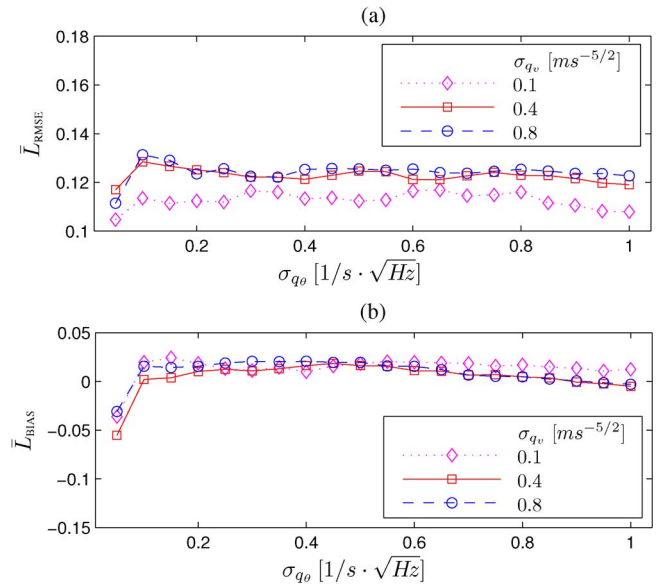
Further research should focus on how to compensate for e.g., multipath effects and GNSS outages, and also investigate the possibility to utilize IMU measurements.

APPENDIX I

We denote the covariance and gain matrix of the process noise (see (21)) by

$$\mathbf{Q}_n \triangleq \begin{bmatrix} \mathbf{Q}_n^{(1)} & \mathbf{0}_{6,2} \\ \mathbf{0}_{2,6} & \mathbf{Q}_n^{(2)} \end{bmatrix}, \quad \text{and} \quad \mathbf{G} \triangleq \begin{bmatrix} \mathbf{I}_8 \\ \mathbf{0}_{2,8} \end{bmatrix}, \qquad (29)$$

respectively. The submatrices are defined by

$$\mathbf{Q}_n^{(1)} \triangleq \begin{bmatrix} \mathbf{Q}_n^{(p)} & \mathbf{Q}_n^{(p,v)} & \mathbf{Q}_n^{(p,\theta)} \\ (\mathbf{Q}_n^{(p,v)})^{\mathsf{T}} & \mathbf{Q}_n^{(v)} & \mathbf{0}_2 \\ (\mathbf{Q}_n^{(p,\theta)})^{\mathsf{T}} & \mathbf{0}_2 & \mathbf{Q}_n^{(\theta)} \end{bmatrix}, \text{ and } \mathbf{Q}_n^{(2)} \triangleq \sigma_{w_p}^2 \mathbf{I}_2. \tag{30}$$

First, note that [44]

$$\mathbf{Q}_n^{(j)} \triangleq \frac{\sigma_{q_j}^2}{2\alpha_j^3} \begin{bmatrix} (e^{\alpha_j \Delta t_n} - 2)^2 + 2\alpha_j \Delta t_n - 1 & \alpha_j (e^{\alpha_j \Delta t_n} - 1)^2 \\ \alpha_j (e^{\alpha_j \Delta t_n} - 1)^2 & \alpha_j^2 (e^{2\alpha_j \Delta t_n} - 1) \end{bmatrix} \tag{31}$$

for $j = v, \theta$. Now, integrating the true integral equal to the relative position $\Delta \mathbf{p}_{n+1}$, linearizing the integrand, and approximating the integral according to the trapezoidal rule, we obtain

$$\begin{aligned} \Delta \mathbf{p}_{n+1} &= \int_{t_n}^{t_{n+1}} v(t) \begin{bmatrix} \cos(\theta(t)) \\ \sin(\theta(t)) \end{bmatrix} dt \\ &\approx \int_{t_n}^{t_{n+1}} v_n \begin{bmatrix} \cos(\theta_n) \\ \sin(\theta_n) \end{bmatrix} dt + \int_{t_n}^{t_{n+1}} (v(t) - v_n) \begin{bmatrix} \cos(\theta_n) \\ \sin(\theta_n) \end{bmatrix} dt \\ &\quad + \int_{t_n}^{t_{n+1}} (\theta(t) - \theta_n) v_n \begin{bmatrix} -\sin(\theta_n) \\ \cos(\theta_n) \end{bmatrix} dt \\ &\approx \frac{\Delta t_n}{2} \left(v_n \begin{bmatrix} \cos(\theta_n) \\ \sin(\theta_n) \end{bmatrix} - v_n \theta_n \begin{bmatrix} -\sin(\theta_n) \\ \cos(\theta_n) \end{bmatrix} \right. \\ &\quad \left. + \begin{bmatrix} \cos(\theta_n) & -v_n \sin(\theta_n) \\ \sin(\theta_n) & v_n \cos(\theta_n) \end{bmatrix} \begin{bmatrix} v_{n+1} \\ \theta_{n+1} \end{bmatrix} \right). \end{aligned} \tag{32}$$

Rewriting $[v_{n+1} \; \theta_{n+1}]^{\mathsf{T}}$ according to (13) we arrive at

$$\Delta \mathbf{p}_{n+1} = \mathbf{f}_p(\mathbf{x}_n) + \mathbf{S} \begin{bmatrix} [\mathbf{q}_n]_3 \\ [\mathbf{q}_n]_5 \end{bmatrix} \tag{33}$$

where $\mathbf{f}_p(\mathbf{x}_n)$ replaces the topmost rows of $\mathbf{f}(\mathbf{x}_n)$ in the implementation, $[\mathbf{c}]_n$ denotes element n in the vector $\mathbf{c}$, and

$$\mathbf{S} \triangleq \frac{\Delta t_n}{2} \begin{bmatrix} \cos(\theta_n) & -v_n \sin(\theta_n) \\ \sin(\theta_n) & v_n \cos(\theta_n) \end{bmatrix}. \tag{34}$$

The corresponding process noise is given by

$$\mathbf{Q}_n^{(p)} \triangleq \mathbf{S} \begin{bmatrix} [\mathbf{Q}_n^{(v)}]_{1,1} & 0 \\ 0 & [\mathbf{Q}_n^{(\theta)}]_{1,1} \end{bmatrix} \mathbf{S}^{\mathsf{T}} \tag{35}$$

with $[\mathbf{M}]_{n_1, n_2}$ denoting the element at row n_1 and column n_2 in the matrix $\mathbf{M}$. By similar reasoning, we have

$$\mathbf{Q}_n^{(p,v)} \triangleq \frac{\Delta t_n}{2} \begin{bmatrix} \cos(\theta_n) \\ \sin(\theta_n) \end{bmatrix} \begin{bmatrix} [\mathbf{Q}_n^{(v)}]_{1,1} & [\mathbf{Q}_n^{(v)}]_{1,2} \end{bmatrix} \tag{36}$$

$$\mathbf{Q}_n^{(p,\theta)} \triangleq \frac{v_n \Delta t_n}{2} \begin{bmatrix} -\sin(\theta_n) \\ \cos(\theta_n) \end{bmatrix} \begin{bmatrix} [\mathbf{Q}_n^{(\theta)}]_{1,1} & [\mathbf{Q}_n^{(\theta)}]_{1,2} \end{bmatrix}. \tag{37}$$

REFERENCES

[1] V. Cherian et al., "Model-based design of a SUV anti-rollover control system," presented at the Proc. SAE World Congr., Detroit, MI, USA, Apr. 2008, SAE Tech. Paper 2008-01-0579.

[2] U.S. Department of Transportation, "Rollover data special study final report," Nat. Highway Traffic Safety Admin., Washington, DC, USA, Tech. Rep., Jan. 2011.

[3] "Insurance telematics, global study: Free abstract," Ptolemus Consulting Group, Paris, France, Tech. Rep., 2013.

[4] "Insurance Telematics Report 2013," Telematics update, 2013.

[5] P. Händel et al., "Insurance telematics: Opportunities and challenges with the smartphone solution," IEEE Intell. Transp. Syst. Mag., vol. 5, no. 4, pp. 57–70, Oct. 2014.

[6] C. Saiprasert and W. Pattara-Atikom, "Smartphone enabled dangerous driving report system," in Proc IEEE Int. Conf. Syst. Sci., Maui, HI, USA, Jan. 2013, pp. 1231–1237.

[7] H. Eren, S. Makinist, E. Akin, and A. Yilmaz, "Estimating driving behavior by a smartphone," in Proc. IEEE Int. Veh. Symp., Alcalá de Henares, Spain, Jun. 2012, pp. 234–239.

[8] D. Johnson and M. Trivedi, "Driving style recognition using a smartphone as a sensor platform," in Proc. IEEE Conf. Intell. Transp. Syst., Washington, DC, USA, Oct. 2011, pp. 1609–1615.

[9] J. Meseguer, C. Calafate, J. Cano, and P. Manzoni, "Drivingstyles: A smartphone application to assess driver behavior," in Proc. IEEE Symp. Comput. Commun., Split, Croatia, Jul. 2013, pp. 535–540.

[10] I. Aicardi, P. Dabove, A. Lingua, and M. Piras, "Sensors integration for smartphone navigation: Performances and future challenges," in Proc. ISPRS Tech. Commiss. III Symp., Zurich, Switzerland, Sep. 2014, pp. 9–16.

[11] P. Händel, J. Ohlsson, M. Ohlsson, I. Skog, and E. Nygren, "Smartphone-based measurement systems for road vehicle traffic monitoring and usage-based insurance," IEEE Syst. J., vol. 8, no. 4, pp. 1238–1248, Dec. 2014.

[12] J. C. Herrera et al., "Evaluation of traffic data obtained via GPS-enabled mobile phones: The mobile century field experiment," Transp. Res. C, Emerging Technol., vol. 18, no. 4, pp. 568–583, Aug. 2010.

[13] P. Mazare, O. Tossavainen, and D. Work, "Computing travel times from filtered traffic states," Discr. Continuous Dy. Syst.—Ser. S, vol. 7, no. 3, pp. 557–578, Jun. 2014.

[14] R. Wang, D. Work, and R. Sowers, "Multiple model particle smoothing for traffic incident detection," IEEE Trans. Intell. Transp. Syst., submitted for publication.

[15] B. Hardjono, A. Wibowo, M. Rachmadi, and W. Jatmiko, "Mobile phones as traffic sensors with map matching and privacy considerations," in Proc. IEEE Int. Symp. Micro-Nano Mechatron. Human Sci., Nagoya, Japan, Nov. 2012, pp. 450–455.

[16] X. Gao et al., "Elastic pathing: Your speed is enough to track you," in Proc. ACM Int. Joint Conf. Pervasive Ubiquitous Comput., Seattle, WA, USA, Sep. 2014, pp. 975–986.

[17] "Telematics insurance—A disruptive innovation," IBM Global Business Serv., Armonk, NY, USA, Tech. Rep., 2012.

[18] O. Walter, J. Schmalenstroeer, A. Engler, and R. Haeb-Umbach, "Smartphone-based sensor fusion for improved vehicular navigation," in Proc. 10th WPNC, Dresden, Germany, Mar. 2013, pp. 1–6.

[19] R. Munguia and A. Grau, "A practical method for implementing an attitude and heading reference system," Int. J. Adv. Robot Syst., vol. 11, no. 62, pp. 1–12, Apr. 2014.

[20] P. D. Groves, Principles of GNSS, Inertial, and Multisensor Integrated Navigation Systems, 1st ed. Norwood, MA, USA: Artech House, 2008.

[21] J. Paefgen, F. Kehr, Y. Zhai, and F. Michahelles, "Driving behavior analysis with smartphones: Insights from a controlled field study," in Proc. 11th Mobile Ubiquitous Multimedia Conf., Luleå, Sweden, Dec. 2012, pp. 36:1–36:8.

[22] S. Ayub, A. Bahraminasab, and B. Honary, "A sensor fusion method for smart phone orientation estimation," in *Proc. 13th Annu. Symp. Convergence Telecommun., Netw. Broadcast.*, Liverpool, U.K., Jun. 2012.

[23] X. Niu, Q. Zhang, Y. Li, Y. Cheng, and C. Shi, "Using inertial sensors of iPhone 4 for car navigation," in *Proc. IEEE/ION Position, Location Navig. Symp.*, Myrtle Beach, SC, USA, Apr. 2012, pp. 555–561.

[24] J. Farrell, *Aided Navigation: GPS With High Rate Sensors*, 1st ed. New York, NY, USA: McGraw-Hill, 2008.

[25] I. Skog and P. Händel, "In-car positioning and navigation technologies—A survey," *IEEE Trans. Intell. Transp. Syst.*, vol. 10, no. 1, pp. 4–21, Mar. 2009.

[26] N. Mutoh and T. Takayanagi, "Cornering performance of front and rear wheel independent drive type electric vehicles (FRID EVs) under severe road conditions," in *Proc. IEEE Conf. Intell. Transp. Syst.*, Washington, DC, USA, Oct. 2011, pp. 101–106.

[27] D. Bevly, J. Ryu, and J. Gerdes, "Integrating INS sensors with GPS measurements for continuous estimation of vehicle sideslip, roll, and tire cornering stiffness," *IEEE Trans. Intell. Transp. Syst.*, vol. 7, no. 4, pp. 483–493, Dec. 2006.

[28] H. Slimi, H. Arioui, and S. Mammar, "Motorcycle lateral dynamic estimation and lateral tire-road forces reconstruction using sliding mode observer," in *Proc. IEEE Conf. Intell. Transp. Syst.*, Hague, The Netherlands, Oct. 2013, pp. 584–589.

[29] M. C. Walz, "Trends in the static stability factor of passenger cars, light trucks, and vans," U.S. Dept. Transp., Washington, DC, USA, Tech. Rep., Jun. 2005.

[30] D. N. Penny, "Rollover of sport utility vehicles," *Phys. Teacher*, vol. 42, no. 2, pp. 86–91, Jan. 2004.

[31] M. Doumiati, A. Victorino, A. Charara, and D. Lechner, "Lateral load transfer and normal forces estimation for vehicle safety: Experimental test," *Veh. Syst. Dyn.*, vol. 47, no. 12, pp. 1511–1533, Nov. 2009.

[32] F. Gustafsson, "Slip-based tire-road friction estimation," *Automatica*, vol. 33, no. 6, pp. 1087–1099, Jun. 1997.

[33] M. Reineh, M. Enqvist, and F. Gustafsson, "Detection of roof load for automotive safety systems," in *Proc. IEEE Conf. Decision Control*, Florence, Italy, Dec. 2013, pp. 2840–2845.

[34] G. Phanomchoeng and R. Rajamani, "Real-time estimation of rollover index for tripped rollovers with a novel unknown input nonlinear observer," *IEEE/ASME Trans. Mechatronics*, vol. 19, no. 2, pp. 743–754, Apr. 2014.

[35] P. Girling, Ed. *Automotive Handbook*, 4th ed. Gerlingen, Germany: Robert Bosch GmbH, 1996.

[36] B. P. Gibbs, *Advanced Kalman Filtering, Least-Squares and Modeling: A Practical Handbook*, 1st ed. Hoboken, NJ, USA: Wiley, 2011.

[37] L. Serrano, D. Kim, and R. Langley, "A GPS velocity sensor: How accurate can it be?" in *Proc. ION NTM*, San Diego, CA, USA, Jan. 2004, pp. 877–885.

[38] E. D. Kaplan and C. J. Hegarty, *Understanding GPS-Principles and Applications*. Norwood, MA, USA: Artech House, 2006.

[39] S. Kolås, B. Foss, and T. Schei, "Constrained nonlinear state estimation based on the UKF approach," *Comput. Chem. Eng.*, vol. 33, no. 8, pp. 1386–1401, Aug. 2009.

[40] F. Gustafsson, *Statistical Sensor Fusion*, 1st ed. Lund, Sweden: Studentlitteratur, 2010.

[41] K. Pfleger, retrieved 2014-07-06. [Online]. Available: http://www.ksl.stanford.edu/people/kpfleger/auto/handling.html

[42] S. Julier and J. LaViola, "On Kalman filtering with nonlinear equality constraints," *IEEE Trans. Signal Process.*, vol. 55, no. 6, pp. 2774–2784, Jun. 2007.

[43] "NAVSTAR GPS—User equipment introduction," U.S. Dept. Defense, Arlingto, VA, USA, Public Release Version, Tech. Rep., Sep. 1996.

[44] J. Wahlström, I. Skog, and P. Händel, "Risk assessment of vehicle cornering events in GNSS data driven insurance telematics," in *Proc. IEEE Conf. Intell. Transp. Syst.*, Qingdao, China, Oct. 2014, pp. 3132–3137.

Johan Wahlström received the M.Sc. degree in engineering physics from KTH Royal Institute of Technology, Stockholm, Sweden, in 2014. He is currently working toward the Ph.D. degree in the Department of Signal Processing, KTH Royal Institute of Technology. His main research topic is insurance telematics.

Isaac Skog (S'09–M'10) received the B.Sc. and M.Sc. degrees in electrical engineering and the Ph.D. degree in signal processing, with a thesis on low-cost navigation systems, from KTH Royal Institute of Technology, Stockholm, Sweden, in 2003, 2005, and 2010, respectively. In 2009, he was a Visiting Researcher for five months with the Mobile Multi-Sensor System Research Team, University of Calgary, Calgary, Canada. In 2011, he was a Visiting Scholar for four months at the Indian Institute of Science, Bangalore, India. He is currently a Researcher at KTH Royal Institute of Technology, coordinating the KTH Insurance Telematics Lab. Dr. Skog was a recipient of a Best Survey Paper Award by the IEEE Intelligent Transportation Systems Society in 2013.

Peter Händel (S'88–M'94–SM'98) received the Ph.D. degree from Uppsala University, Uppsala, Sweden, in 1993. From 1987 to 1993, he was with Uppsala University. From 1993 to 1997, he was with Ericsson AB, Kista, Sweden. From 1996 to 1997, he was a Visiting Scholar with Tampere University of Technology, Tampere, Finland. Since 1997, he has been with KTH Royal Institute of Technology, Stockholm, Sweden, where he is currently a Professor of signal processing and the Head of the Department of Signal Processing. From 2000 to 2006, he held an adjunct position at the Swedish Defence Research Agency. He has been a Guest Professor at the Indian Institute of Science, Bangalore, India, and at the University of Gävle, Gävle, Sweden. He is a Cofounder of Movelo AB. Dr. Händel has served as an Associate Editor of the IEEE TRANSACTIONS ON SIGNAL PROCESSING. He was a recipient of a Best Survey Paper Award by the IEEE Intelligent Transportation Systems Society in 2013.